frontiers | Frontiers in Chemistry

TYPE Original Research
PUBLISHED 14 December 2022
DOI 10.3389/fchem.2022.1111435

OPEN ACCESS

EDITED BY
Chao Liu,
Yancheng Institute of Technology, China

REVIEWED BY
Xiaolei Yuan,
Nantong University, China
Jinchen Fan,
University of Shanghai for Science and Technology, China

*CORRESPONDENCE
Yiting Peng,
pyt_1108@shiep.edu.cn

SPECIALTY SECTION
This article was submitted to Catalytic Reactions and Chemistry, a section of the journal Frontiers in Chemistry

RECEIVED 29 November 2022
ACCEPTED 05 December 2022
PUBLISHED 14 December 2022

CITATION
Yu W, Geng N, Han J, Yu W and Peng Y (2022), Mesoporous crystalline $Ti_{1-x}Sn_xO_2$ ($0 < x < 1$) solid solution for a high-performance photocatalyst under visible light irradiation.
Front. Chem. 10:1111435.
doi: 10.3389/fchem.2022.1111435

Mesoporous crystalline $Ti_{1-x}Sn_xO_2$ ($0 < x < 1$) solid solution for a high-performance photocatalyst under visible light irradiation

Wen Yu, Nankun Geng, Jianming Han, Wenjun Yu and Yiting Peng*

Shanghai Key Laboratory of Materials Protection and Advanced Materials in Electric Power, Shanghai University of Electric Power, Shanghai, China

We report a facile and effective inorganic polycondensation combined with aerosol-spray strategy towards high-performance photocatalyst by fabricating mesoporous $Ti_{1-x}Sn_xO_2$ ($0 < x < 1$) solid solution. Such $Ti_{1-x}Sn_xO_2$ nanocrystals with high Sn-doped contents are self-assembled into mesoporous spheres can effectively promote visible-light harvest and high quantum yield, leading a longer lifetime of the photoelectron-hole pairs and less recombination. Such the photocatalysts enhanced photocatalytic activity for the degradation of Rhodamine B (RhB). The representative $Ti_{0.9}Sn_{0.1}O_2$ and $Ti_{0.8}Sn_{0.2}O_2$ compounds reach an optimum degradation of ≈50% and 70%, respectively, after 120 min irradiation under visible irradiation. The mesoporous $Ti_{1-x}Sn_xO_2$ solid solution could inhibit the recombination of electron-hole pairs, which promote reaction thermodynamics and kinetics for RhB degradation.

KEYWORDS

TiO2, solid solution, aerosol-spray, self-assembly, photocatalyst

1 Introduction

Rapid development and the transition to a carbon-neutral society have highlighted the need for photovoltaic cells to use high-efficiency photocatalysts under visible light (>380 nm) (Liu et al., 2016; Galvao et al., 2018; González-Gutiérrez et al., 2019). Transition metal oxides (such as TiO_2 and SnO_2) have attracted considerable attention from researchers due to their excellent photocatalytic activity, high natural abundance, and cost-effectiveness (Sharon et al., 2016). Owing to two oxides with different band-gap energies (E_g) of 3.2 eV for TiO_2 and 3.8 eV for SnO_2 (Nuansing et al., 2006), respectively, the enhanced charge separation occurs in their mixture where electrons are injected from the conduction band of SnO_2 to the valence band of TiO_2, leading to better performance than individual semiconductor oxides due to their synergistic effects. To better regulate their band gap and obtain high efficiency, more efforts should be focused on building a desired heterostructure and tuning electron

correlation by varying the stoichiometry of oxides Luo et al. (2018). Heterostructures were mainly fabricated by the assembly of two or more oxides that were physically (e.g., Van der Wall's force) or chemically bonded together, exhibiting superiority of geometry and junction interface (Li et al., 2021; Liu et al., 2023). For heterostructure-based metal oxide, element doping coupled with hierarchy design achieved visible benefits due to the formation of a single phase rather than a combination of two oxide compounds. For example, the pre-synthesized SnO_2 quantum dots directed growth on titania show slow charge transfer, low active-sensitizer loading and poor uniformity control for deposition on high aspect-ratio TiO_2 nanostructures (Wang et al., 2022). Doping titania with either inorganic or metallic species can generate donor or acceptor states in the band gap of TiO_2 and impurity states that enhance visible-light adsorption (Albornoz et al., 2021; Wu et al., 2022). Non-etheless, metal oxides with doping heterostructure often suffered from thermal instability, fast recombination rates, or the requirement of an expensive ion-implantation facility for more elaborate control, and even showed much larger formation energy due to the substitution of large-radius metal ions (Singh et al., 2021; Liu et al., 2022). Many essential questions remain, such as the effect of the structure-function correction, composition, and interfaces on the photocatalytic activity, which remains challenging.

One promising strategy to obtain a heterostructure-based titania photocatalyst is to fabricate a substitutional solid solution using metal atoms with a comparable ionic radius (VI-coordinated) with titania (Reddy et al., 2008). Such a metal-doped TiO_2 solid not only retains the benefits from the quantum structures of crystalline titania during photocatalytic processes but further enhances photoinduced surface redox reactions one. Compared with the other cationic doping (such as Cr, V, and Fe), Sn ion shows a more favorable effect on photocatalytic activity in water-splitting and oxidation of organic compounds (Liang et al., 2012). To date, few examples of tin-doping titania (denoted as $Ti_{1-x}Sn_xO_2$, $0 < x < 1$) have been reported, especially on nanoscale systems (Asokan et al., 2010). Such compounds have been generally synthesized by solid-state reaction at high temperatures beyond 1,200°C or chemical deposition technology, such as hydrothermal (Chen et al., 2022; Zhao et al., 2016; Ruiz Esquius et al., 2020), sol-gel (Pudukudy et al., 2017; Liu et al., 2019), electrospinning (Yu et al., 2018), and polyol-mediated methods (Pelicano et al., 2022). However, these methods are limited because of the difficulty in elaborate control of doping contents and nanoparticle aggregation and the incapability of constructing hierarchical pore structures, leading to an increased probability of recombination. Besides, most compounds prepared using the above-mentioned methods have a rutile tetragonal crystalline structure with no anatase analog due to the existence of Sn (Qin et al., 2021). The latter has been proposed to have higher photoactivity than the former, but it is still limited by a less Sn-doping content (<0.3).

To address this challenge, we report a facile and effective doping method to prepare a hierarchically mesoporous $Ti_{1-x}Sn_xO_2$ compound for high-performance photocatalyst under visible light irradiation. Inspired by the Ziegler-Natta catalyst mechanism, Figure 1 illustrates an inorganic polycondensation process that occurs between titanium chloride and tin chloride liquid in a liquid nitrogen bath. The ultra-low temperature effectively suppresses chloride salt hydrolysis and causes chloride ions from tin chloride to fill the empty orbital of a 6-coordinated Ti atom. Then, Ti atoms and Sn atoms were bridged to two chlorine atoms to obtain successive -Ti-Cl-Sn-Cl-Ti- chains, allowing for high Sn-contents. Subsequently, the mesoporous $Ti_{1-x}Sn_xO_2$ spheres are synthesized using a low-cost aerosol-spray method. $Ti_{1-x}Sn_xO_2$ nanocrystals generated from such a preformed aqueous solution are self-assembled into mesoporous spheres. Such a hierarchical heterostructure endows several advantages to the $Ti_{1-x}Sn_xO_2$ compound. Firstly, mesoporous $Ti_{1-x}Sn_xO_2$ spheres inherit the anatase crystalline structure from titania and small nanocrystal size, which achieves a high surface area and many active sites. Second, hierarchically porous architecture coupled with high Sn-contents can effectively promote visible-light harvest and high quantum yield. Finally, the mesoporous structure throughout the spheres endows effective transport of charge carriers, allowing for longer lifetimes of the photoelectron-hole pairs and less recombination. Such a strategy could be easily extended to other photocatalyst designs and large-scale fabrication.

2 Experiment section

2.1 Materials preparation

Pluronic surfactant F127 (EO106PO70EO106), titanium chloride ($TiCl_4$; ≥98%), and tin (IV) chloride ($SnCl_4$, ≥99%) were purchased from Sigma-Aldrich Corp. All chemicals were used without further purification. The $Ti_{1-x}Sn_xO_2$ ($0 < x < 1$) solid solutions and the undoped TiO_2, SnO_2 were all synthesized by an aerosol-spraying process using $TiCl_4$, $SnCl_4$ and tri-block copolymer F127 aqueous solution as a precursor. Such a stable and homogeneous precursor was achieved by a polycondensation process using various mole ratios (Ti: Sn = 1-x: x ($0 < x < 1$) under liquid nitrogen for 2 h and then slowly injecting 100 ml of F127 (0.5 g) aqueous solution. The mole fraction of Sn-containing precursor in the mixture is denoted by x = mmol Sn/(mmol Ti + mmol Sn). The mixture solution was vigorously stirred for 30 min and subsequently used an aerosol-assisted self-assembly process to continuously generate droplets from the precursors. The droplets were then sent through a furnace and reacted at 450°C to form homogenous particles. Calcination was carried out in a box furnace at 350°C for 3 h and then 550°C for another 3 h under the air atmosphere. The heating rate for the

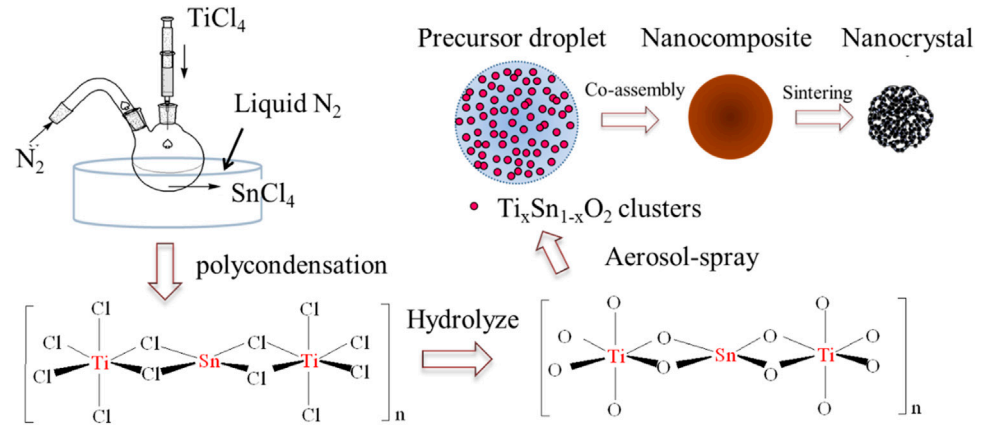

FIGURE 1
Schematic representation of the mesoporous $Ti_{1-x}Sn_xO_2$ ($0 \le x \le 1$) nanocomposites.

whole process was kept at 2°C·min^{-1}. As-made products were milled and grounded into fine powder.

2.2 Material characterization and measurement

X-ray diffraction (XRD) patterns were taken on a Panalytical X'Pert Pro X-ray powder diffractometer powders diffractometer using copper *Kα* radiation (λ = 1.54 Å). Nitrogen sorption isotherms were measured at 77 K with a Micromeritics ASAP 2020 analyzer. The samples were degassed in vacuum at 180°C for 3 h before measurements were taken. The specific surface areas were calculated by the Brunauer–Emmett–Teller (BET) method using the adsorption branch in the relative pressure range from 0.04 to 0.25. The pore size distributions (D_p) were derived from the adsorption branch using the Barrett–Joyner–Halenda (BJH) model. Scanning electron microscopy (SEM) images and energy-dispersive spectroscopy (EDX) were obtained using a JEOL JSM-6700 FE-SEM at 200 kV to obtain morphology and elemental information of the products. Transmission electron microscopy (TEM) images were obtained using a Philips CM120 microscope operated at 120 kV. Surface composition was analyzed by X-ray photoelectron spectroscopy (XPS). Core level photoemission spectra of C 1 s and O 1 s lines were collected with a PHI 3057 spectrometer using Mg *Kα* X-rays at 1,286.6 eV. All XPS spectra were taken in small area mode with an acceptance angle of 78° and 23.5 eV pass energy. All spectra were referenced to the C 1 s peak of the graphitic carbon atom at 285.0 eV. The integrated areas of the Ti 2*p* and Sn 3 days photoemission peaks, divided by their sensitivity factors 0.665/1.334 and 3.286/4.725, were used to determine surface atomic percentages. UV-vis absorption spectra were recorded on a Shimadzu UV-1700 spectrometer with a resolution of 2.0 nm.

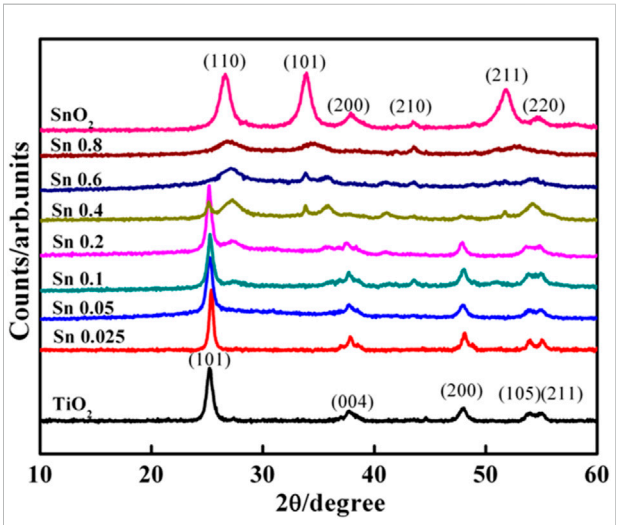

FIGURE 2
XRD curves of the TiO_2, $Ti_{1-x}Sn_xO_2$ and SnO_2 nanocrystals prepared by aerosol method.

2.3 Photocatalytic activity measurement

Under visible light irradiation, the photocatalytic activities of the $Ti_{1-x}Sn_xO_2$ ($0 < x < 1$) solutions were evaluated by the photodegradation of organic contaminants, and Rhodamine B (RhB, M_w: 479.02) was used as the model pollutant. A set of photocatalytic activity experiments on samples were performed with the following procedures: 0.1 g of photocatalyst was put into 30 ml of DI-water and stirred at room temperature for 1 h to make the photocatalyst powder uniformly dispersed. Then RhB was added into the suspension

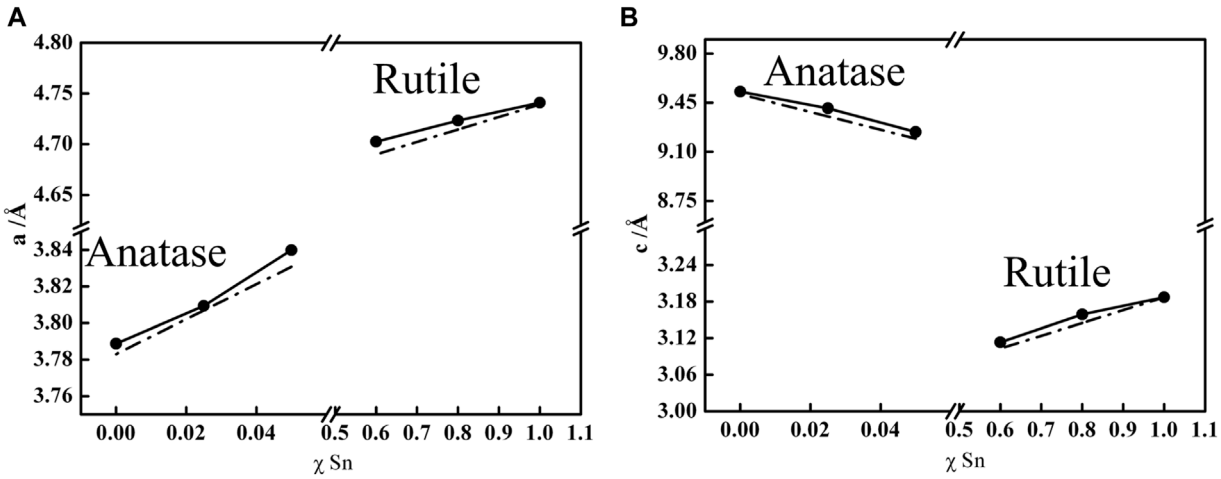

FIGURE 3
Dependence of the mole fraction of Sn (χ) on the *a* **(A)** and *c* **(B)** lattice parameters of $Ti_{1-x}Sn_xO_2$ (0 < x < 1) solid solution (solid lines). Dash dot lines represent the theoretical values according to Vegard's law calculation.

to keep a concentration of 10^{-5} mol·L^{-1}. Then the mixture was stirred in the dark for 30 min to reach adsorption–desorption equilibrium. From the top, the suspension was vertically irradiated with simulated visible light from a 500 W Xe lamp equipped with a UV cutoff filter (>400 nm) with distance of 15 cm between the lamp and the suspension surface. During the photo reaction, the samples were collected at different time intervals; 0 min, 10 min, 30 min, 60 min, 90 min, and 120 min for analysis. In order to estimate the photocatalytic stability, a cycle photocatalytic degradation experiment was conducted as follows: the original concentration of RhB dye in the reactor was tuned to 10^{-5} mol·L^{-1} every 120 min as one cycle, and then the samples were picked up at an interval of 45 min for analysis. The concentration of the RhB was determined by monitoring the height of the maximum (λ = 554) of the absorption in UV-vis spectra.

3 Results and discussion

Figure 2 compares the crystallinity of as-synthesized $Ti_{1-x}Sn_xO_2$ nanocrystals with various Sn-doped contents. The diffraction pattern of as-synthesized TiO_2 nanocrystals match well to that of anatase structure with intense (101) (004), and (200) reflections, corresponding to the 25.4°, 37.8° and 48.1° 2θ angles (JCPD No. 04-0477). Consistently, as-synthesized SnO_2 nanocrystals show crystallized rutile structure with well-defined peaks at 25.3° and 27.4°corresponding to (101) and (110) plane (JPCD No. 84-1286), respectively. Upon increasing Sn-doped, the reflection of $Ti_{1-x}Sn_xO_2$ compounds (x ≤ 0.05) almost retain the anatase phase but a shift toward lower 2θ angels (~0.1°) at (101) peak position. While $Ti_{1-x}Sn_xO_2$ (0.05 < x ≤ 0.4) exhibit two crystalline structures with strong anatase and weak rutile, indicative of crystalline phase transition. For $Ti_{1-x}Sn_xO_2$ (0.6 < x ≤ 0.8), their characteristic peak positions are consistent with rutile SnO_2 (110) peaks at 26.6° and anatase TiO_2 reflection gradually disappeared.

To further confirm the $Ti_{1-x}Sn_xO_2$ formed in a single crystalline phase, Figure 3 compares experimental lattice parameters (*a*, *c*) and unit cell volume ($V = ac^2$) of the anatase $Ti_{1-x}Sn_xO_2$ ($x \leq 0.05$) and the rutile $Ti_{1-x}Sn_xO_2$ ($0.5 < x \leq 0.8$) according to Vegard's law (Kong et al., 2019). The Vegard's law is an approximate empirical rule that predicts the relationship between lattice constant and the concentration of the constituent elements solid solution, as describe as:

$$a = x_1 a_1 + (1 - x_1) a_2 \quad (1)$$

where *a* is the lattice parameter for the solid solution, a_1 and a_2 are lattice parameters of individual oxide, and x_1 is the mole fraction of metal ions. Figure 3A shows the linear trend of lattice parameters *a* for the $Ti_{1-x}Sn_xO_2$ compounds, indicating that the hetero-Sn atom-doped into the TiO_2 lattice brings the lattice expansion. Similarly, the lattice parameter *c* of rutile $Ti_{1-x}Sn_xO_2$ with high Sn-contents (0.5 < x ≤ 0.8) retains the identical trend, as shown in Figure 3B. In contrast, the lattice parameters *c* of anatase $Ti_{1-x}Sn_xO_2$ with low concentration of Sn-contents shows linearly decrease, implying large anisotropy compressibility occurs throughout anatase TiO_2 crystal. The different compressibility (κ, $\kappa_a > \kappa_c$) causes more denser cell lattice with increasing Sn contents, which is consistent with impact of the external stress on solid solution structure (Prasad and Mikula, 2000). Additionally, the phase separation may cause

TABLE 1 The summary of lattice parameters of (101), rutile (110) and (101) plane from anatase lattice; and mass fraction of rutile phase (W_R).

Sample	Peak position (2θ)			Mass fraction of rutile (wt%) W_R
	A (101)	R (110)	R (101)	
TiO_2	25.3°			0.0
$Ti_{0.975}Sn_{0.025}O_2$	25.3°			0.0
$Ti_{0.95}Sn_{0.05}O_2$	25.2°			0.0
$Ti_{0.9}Sn_{0.1}O_2$	25.2°	27.4°		14.8
$Ti_{0.8}Sn_{0.2}O_2$	25.2°	27.3°		19.7
$Ti_{0.6}Sn_{0.4}O_2$	25.1°	27.4°	35.8°	60.6
$Ti_{0.4}Sn_{0.6}O_2$		27.1°	34.8°	100
$Ti_{0.2}Sn_{0.8}O_2$		26.9°	34.5°	100
SnO_2		26.6°	33.9°	100

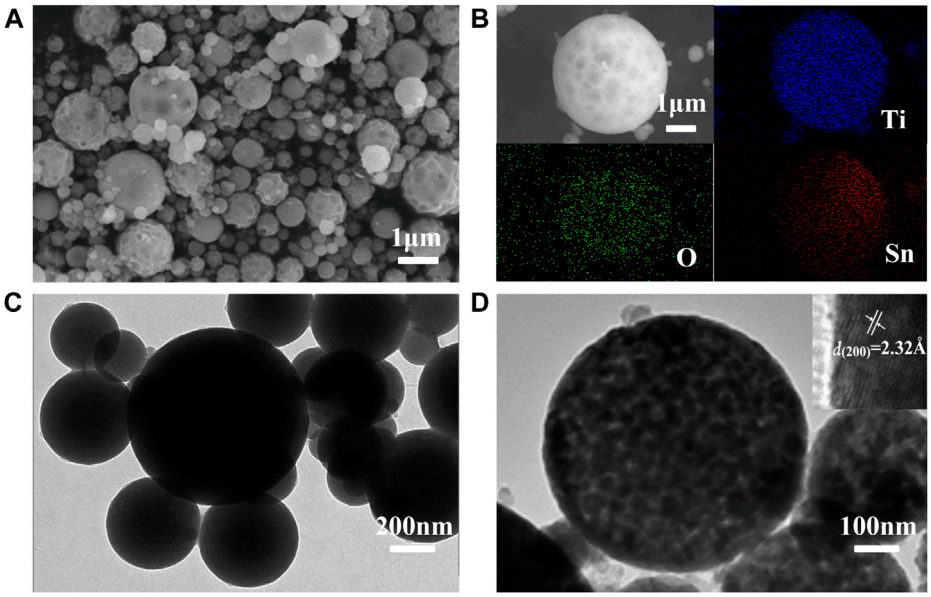

FIGURE 4
(A,B) SEM and elemental mapping images and **(C,D)** TEM images of the $Ti_{0.8}Sn_{0.2}O_2$ solid-solution after sintering at 550°C for 3 h.

certain positive deviate on due to spinodal deposition. Table 1 summarized the anatase-rutile phase distribution of TiO_2, $Ti_{1-x}Sn_xO_2$ ($0 < x < 1$), and SnO_2 according to calculation of the lattice parameters and mass fraction of rutile phase.

$$Sn^{2+} + O_2 + 2H_2O + 2e^- \rightarrow Sn^{4+} + 4OH^- \quad (2)$$

where W_R is the mass fraction of rutile phase, I_R is correction factor which indicates the difference of scattering intensities between crystalline structures, and I_A and I_R represent the integrated intensities of the anatase (101) and rutile (110) reflection, respectively. The mass fraction of rutile phase continuously increases from 14.8 wt% for $Ti_{0.9}Sn_{0.1}O_2$ to 60.6 wt% for $Ti_{0.4}Sn_{0.1}O_2$. Indeed, Sn atoms in TiO_2 lattices could provide large number of dissimilar boundaries, which would suppress the crystal growth of TiO_2 in the dealloying process, finally leading to extremely fine nanostructure in TiO_2-SnO_2 solid solution (Sayılkan et al., 2008; Wu et al., 2017). Hence, such a series of $Ti_{1-x}Sn_xO_2$ ($0 < x < 1$) compounds underwent pure anatase, mixed anatase-rutile to pure rutile phases, respectively, which provide a fundamental understanding of

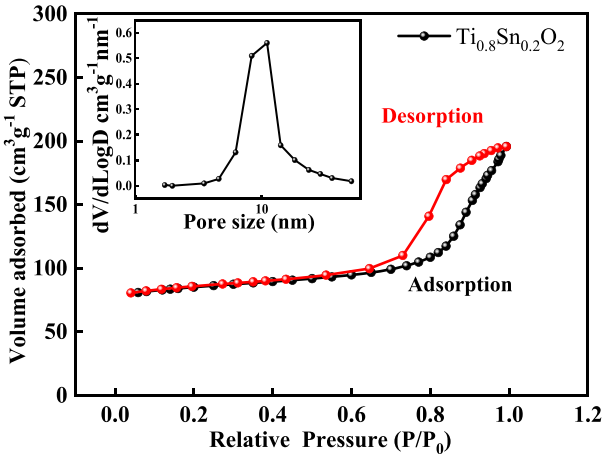

FIGURE 5
Nitrogen sorption isotherms and pore size distribution (inset) of the $Ti_{0.8}Sn_{0.2}O_2$ compound.

the relationship between electronic structure and dye-sensitized photocatalytic degradation.

The morphology and elements analysis of $Ti_{1-x}Sn_xO_2$ ($0 < x < 1$) compounds obtained after self-assembly are characterized by scanning electron microscope (SEM) combined with energy-dispersive X-ray (EDX), as shown in Figures 4A,B. All samples show similarly spherical morphology with a diameter range from 150 to 500 nm, exemplified by $Ti_{0.8}Sn_{0.2}O_2$. The bestrewed pot-holes on the spheres surface are also observed arising from the stacking of hard-sphere crystals. The uniform distribution of each element suggests that the presence of Ti and Sn atoms throughout crystalline structure. Transmission electron microscopic (TEM) image clearly displays the as-sprayed $Ti_{0.8}Sn_{0.2}O_2$ particles with non-porous spherical morphology before sintering (Figure 4C). After sintering, the compounds become highly porous due to removal of surfactant, and each sphere is composed of uniform nanocrystals with diameter around 5–6 nm. High-resolution TEM (HRTEM) in Figure 4D shows the ultrafine nanocrystals with an interlayer spacing of 2.32 Å, corresponding to the (200) plane of rutile TiO_2 (~2.29 Å). This result is consistent with the XRD patterns, showing initial extension of *c* axis occurs during the anatase-rutile conversion at higher Sn-contents doping. Such hierarchically porous design and highly crystalline structure can provide high surface area and fast kinetics, which favors the transport of charge carriers and prevent the recombination of photoelectron-hole pairs.

Nitrogen sorption experiment was further conducted to probe the pore structure. Figure 5 shows the nitrogen sorption isotherms and pore size distribution of anatase $Ti_{0.8}Sn_{0.2}O_2$ solid solution with rutile-phased fraction of 20 wt%, confirming a hierarchical pore structure including micropore, mesopore, and macropores arising from particles aggregation. The significant nitrogen uptake at the relative pressures at 0.4–0.6 is consistent with a mesopore network with a narrow pore distribution of ~10 nm (inset). Table 2 summarizes the surface area and pore structure parameters of $Ti_{1-x}Sn_xO_2$ ($0 < x \leq 0.4$). Upon increasing the Sn-doped contents, the surface areas of $Ti_{1-x}Sn_xO_2$ compounds shows significantly decrease from 77.58 $m^2 \cdot g^{-1}$–44.96 $m^2 \cdot g^{-1}$ due to introduction of heavier Sn atoms. Additionally, the average pore volumes of $Ti_{1-x}Sn_xO_2$ maintain approximately ~0.15 $cm^2 \cdot g^{-1}$.

To further understand the electronic properties depended transformation between anatase and rutile phase, the elemental composition and valence state in anatase $Ti_{0.95}Sn_{0.05}O_2$ and anatase-rutile $Ti_{0.8}Sn_{0.2}O_2$ are conducted by X-ray photoelectron spectra (XPS), as shown in Figure 6. Figure 6A shows the Ti 2*p* fitting curves for, which presents two Ti 2*p* peaks at E = 458.2 eV and E = 463.7 eV for Ti $2p_{3/2}$ and Ti $2p_{1/2}$ lines, respectively. Which is consistent with the values of Ti^{4+} reported previously (Fan et al., 2021). Meanwhile, Figure 6B represents typical Sn 3*d* curves for $Ti_{0.95}Sn_{0.05}O_2$ and $Ti_{0.8}Sn_{0.2}O_2$ with both peaks at 494.2 eV and 485.9 eV for Sn $3d_{3/2}$ and Sn $3d_{5/2}$ lines, interpolating peak positions of the metallic Sn and SnO_2 at 493.1/495.0 eV and 484.7/486.4 eV for Sn $3d_{3/2}$/Sn $3d_{5/2}$ lines, which can be ascribed to the Sn^{4+} species. These results indicate no changes in valence state of Sn and Ti during phase transformation, implying the distorted degree in tetragonal structure is neglected at low Sn concentration. Together with XPS analysis, Table 3 compares the atomic concentration ratios of O 1*s* and Ti 2*p* for undoped TiO_2, $Ti_{0.95}Sn_{0.05}O_2$ and $Ti_{0.8}Sn_{0.2}O_2$. The concentration ratio of Ti 2*p* to O 1*s* decrease with increasing Sn contents, suggesting the Sn-doped in the tetragonal TiO_2 lattice for formation of Ti-O-Sn bonding.

To demonstrate this intricate structure-function correction, we evaluate the photoactivity of the porous $Ti_{1-x}Sn_xO_2$ ($0.05 \leq x \leq 0.4$) nanoparticles in degradation of RhB dye under visible light irradiation, as shown in Figure 7. The blank experiment showed that the concentration of RhB solution without catalyst maintain during 90 min, indicating the RhB molecules are relatively stable and hard to decompose. Before photocatalytic degradation, it is necessary to the eliminate an adsorption effect by stirring the mixtures in the dark for 1 h. Then the $Ti_{1-x}Sn_xO_2$ compounds were added in RhB solution being treated in the dark for another 60 min. All the samples have strong physical adsorption abilities, but porous solid solution can enhance adsorption ability than the blank samples. After adsorption, the next photocatalytic degradation experiments kept the RhB concentration at equilibrium as the starting point. Upon increasing Sn-doped contents, the $Ti_{0.9}Sn_{0.1}O_2$ and $Ti_{0.8}Sn_{0.2}O_2$ solutions with mixed anatase-rutile phases exhibit the higher photoactivity (RhB degradation yield ≈50% and 70%, respectively after irradiation for 120 min) than that of the anatase $Ti_{0.95}Sn_{0.05}O_2$ solution (RhB degradation yield <10% after irradiation for 120 min). However, the photocatalytic activity of $Ti_{0.6}Sn_{0.4}O_2$ with higher rutile phased of 60 wt% decrease with

TABLE 2 The parameters of pore structure in pure TiO_2 and $Ti_{1-x}Sn_xO_2$ ($0 < x \leq 0.4$).

Sample	Surface area/$m^2 \cdot g^{-1}$	Average pore size/nm	Pore volume/$cm^3 \cdot g^{-1}$
TiO_2	77.58	8.75	0.18
$Ti_{0.95}Sn_{0.05}O_2$	57.28	14.58	0.16
$Ti_{0.9}Sn_{0.1}O_2$	56.00	13.77	0.14
$Ti_{0.8}Sn_{0.2}O_2$	50.06	10.67	0.19
$Ti_{0.6}Sn_{0.4}O_2$	44.96	8.42	0.21

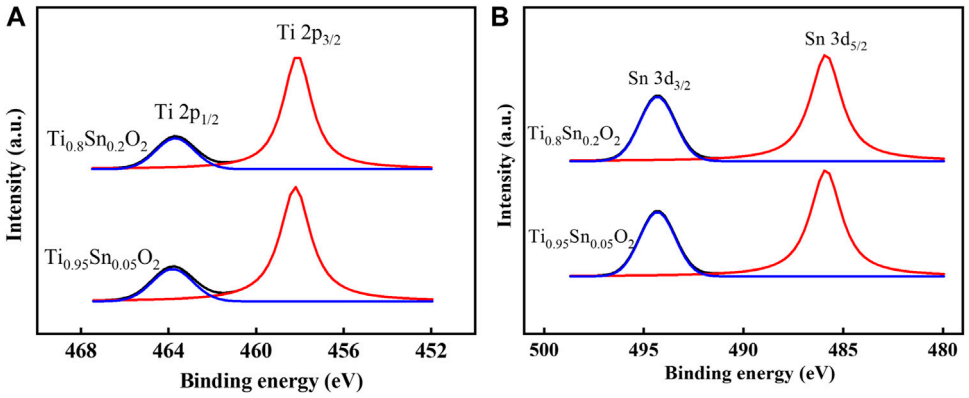

FIGURE 6
XPS curves fitted of **(A)** Ti 2p spectra of $Ti_{0.95}Sn_{0.05}O_2$ and $Ti_{0.8}Sn_{0.2}O_2$, **(B)** Sn 3*d* spectra of $Ti_{0.95}Sn_{0.05}O_2$ and $Ti_{0.8}Sn_{0.2}O_2$.

TABLE 3 States of $Ti_{0.95}Sn_{0.05}O_2$ and $Ti_{0.8}Sn_{0.2}O_2$ solid solution and elemental surface composition determined by XPS.

Sample		TiO_2	$Ti_{0.95}Sn_{0.05}O_2$	$Ti_{0.8}Sn_{0.2}O_2$
BE (eV)	O 1 s	530.3	529.5	529.4
	Ti 2p3/2	459.8	458.2	458.2
	Sn 3d5/2	—	485.9	485.9
Atomic Conc (%)	O 1s	47.3	46.6	45.8
	Ti 2p3/2	17.2	15.3	8.7
	Sn 3d5/2	—	0.8	2.0

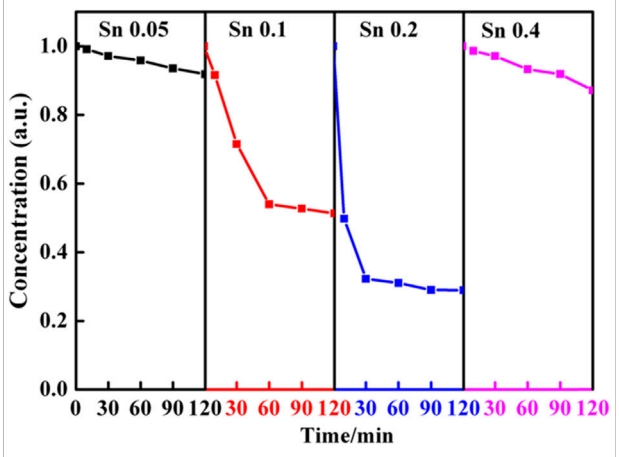

FIGURE 7
Dependence of the Sn-doped contents on the reaction time of $Ti_{1-x}Sn_xO_2$ ($0.05 \leq x \leq 0.4$) compounds with RhB under visible-light harvester.

increasing Sn content because the RhB degradation yield is only about 15% after irradiation for 120 min.

In the heterojunction composed of TiO_2 and SnO_2, the photogenerated electrons can transfer from TiO_2 to SnO_2 phase with no applied voltage (Fan et al., 2016). Because of their identical rutile phase, tetragonal crystal structures, ionic radius (0.690 for Sn^{4+} and 0.605 for Ti^{4+}), and electronic characteristics, SnO_2 and TiO_2 may also form solid solutions coupling system (Sayılkan, 2007; Huang et al., 2015). Thus, it is very essential to probe the relationship between electronic structure and photoactivity in $Ti_xSn_{1-x}O_2$ solutions. Figure 8 illustrates the dependence of band gap of $Ti_{1-x}Sn_xO_2$ ($0 \leq x \leq 1$) with increasing Sn-doping. Theoretical considerations by Long

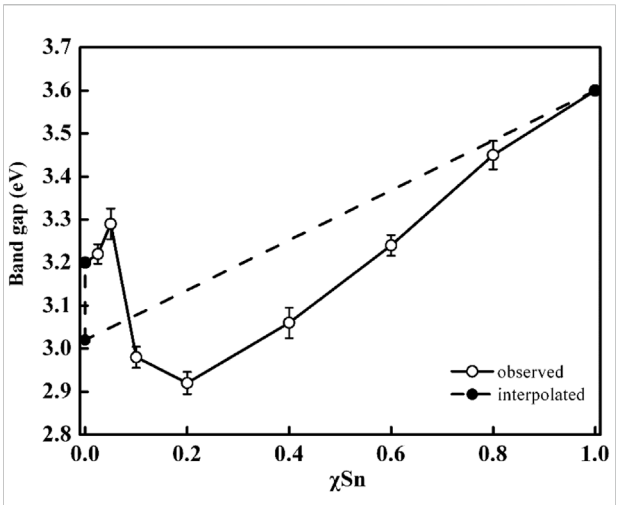

FIGURE 8
Variation in optical band gap of $Ti_{1-x}Sn_xO_2$ (0 < x < 1) samples. Dashed line is a linear interpolation between the band gap values for anatase TiO_2 (3.2 eV), rutile TiO_2 (3.0 eV), and SnO_2 (3.60 eV).

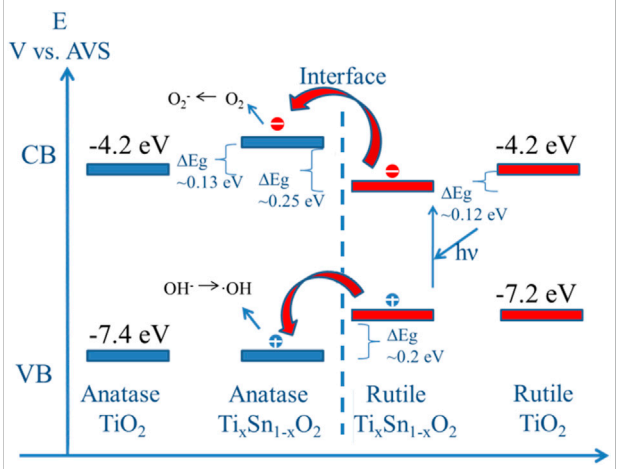

FIGURE 9
Scheme of electron transition between mixed $Ti_{1-x}Sn_xO_2$ ($0.1 \le x \le 0.4$) solutions. The absolute valence band and conduction band edges relative to vacuum level of TiO_2 are obtained from the reference.

et al. suggest that for substitutionally Sn-doped anatase TiO_2, the band gap increases ~0.13 eV owing to high formation energy while maintain anatase phase (Long et al., 2009). However, the substitution of Sn for rutile TiO_2 brings a red-shift of the adsorption edge deriving from the decrease of Sn 5s gap state in the conduction band (Chang et al., 2019). Consistent with the theoretical analysis, the experimental band gaps of the anatase $Ti_{1-x}Sn_xO_2$ (x = 0.05 and 0.025, respectively) solid solutions indeed increase to 3.22 and 3.29 eV, respectively (Ren et al., 2020). High Sn-doped contents causes a transition from anatase to rutile phase, and the band gap of solution with mixed phase should be reasonably neutralized in between that of single phase using their mass fraction (Chen et al., 2010; Mohammad et al., 2021). However, it is worth noting that the band gap values of $Ti_{0.9}Sn_{0.1}O_2$ and $Ti_{0.8}Sn_{0.2}O_2$ decreases to 2.98 and 2.92 eV, respectively. This is possibly attributed to transition of photoexcited electrons and holes from rutile to energy states of anatase phase, which needs very low energy about 0.2~0.25 eV. Meanwhile, we discovered that the presence of crystalline interface within mixed phases effectively reduces electron-hole recombination and creates more oxygen vacancies to enhance visible-light harvesting ability.

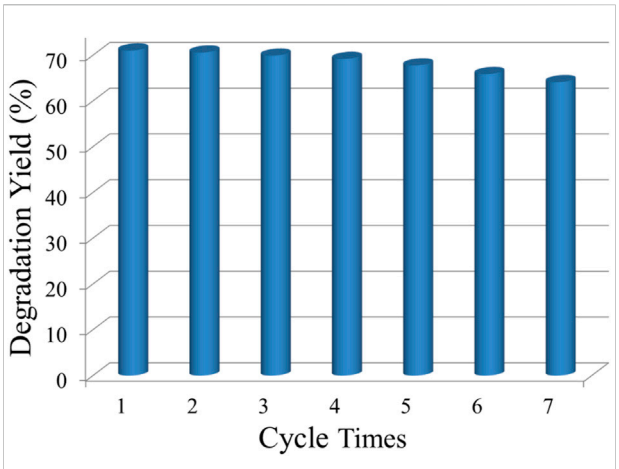

FIGURE 10
Degradation yield of $Ti_{0.8}Sn_{0.2}O_2$ mixed solution after seven cycles.

Continuation of this process gradually separates photoexcited electron-hole pairs, sequentially providing more photo-charges needed for the photocatalytic reaction and fast charge migration, as shown in Scheme of Figure 9. The rapid increased band gap values of $Ti_{1-x}Sn_xO_2$ ($0.4 \le x \le 0.8$) is attributed to the more Sn doping, leading the conduction band to shift toward a higher energy, which accounts for the observed decreasing photocatalytic activity at a higher Sn content (e.g., $x \ge 0.8$). Rather than facilitate charge migration and reduce charge recombination, the charge trapping may take effect as centers for electro-hole recombination and absorb the visible light, described as follow reaction 1 and 2 (Golestanbagh et al., 2018; Shi et al., 2007):

$$Ti^{4+} + e^- \rightarrow Ti^{3+} \quad (1a)$$

$$Sn^{4+} + 2e^- \rightarrow Sn^{2+} \quad (2a)$$

$$O^{2-} \rightarrow O + V_o + 2e^- \quad (3)$$

The visible-spectra sensitization of Sn-doped TiO_2 is attribute from charge transfer bands of peroxotitanium or the

formation of Sn II) with stable lower oxidation state (Serpone., 2006). The loss of O atoms creates the formation of color center due to the charge trapped in cavity (V_o) left behind (reaction 3). Such the impacted effects on visible-light driven reactivity for color centers are even more important than the narrowing band gap caused by doping Bjelajac et al. (2018).

For the improved spectral response in the visible region, the $Ti_{0.8}Sn_{0.2}O_2$ solution also shows relatively stable photodegradation performance, as shown in Figure 10. The preformed powder is centrifuged and collected after every irradiation cycle and subsequently dispersed in a fresh RhB aqueous solution without any further purification. Compare with the first cycle, the photocatalyst displays a less than 10% decrease in activity after seven cycle times, endowing a cycling stability for solution with a mixed phase.

4 Conclusion

In summary, a facile and effective aerosol-spray strategy is developed to prepare high-performance photocatalyst by fabricating mesoporous $Ti_{1-x}Sn_xO_2$ ($0 < x < 1$) solid solution. $Ti_{1-x}Sn_xO_2$ nanocrystals with various Sn-doped contents are self-assembled into mesoporous spheres provide effective transport of charge carrier. As-prepared hierarchical architecture shows several advantages as a visible-light photocatalyst. First, mesoporous $Ti_{1-x}Sn_xO_2$ spheres enhance the advantageous features of conventional titania and tin oxides. Second, heterostructure-based titania compounds further enhance photoinduced surface redox reactions and kinetic process in the visible region. Third, with increasing Sn-doped concentration, the mechanism between the anatase-rutile phase transition of $Ti_{1-x}Sn_xO_2$ compounds and photocatalytic activity is further revealed. Therefore, as-prepared mesoporous $Ti_{1-x}Sn_xO_2$ solid solution can effectively enhanced charge separation, and accelerated proton mass transfer. This demonstration of creating solid solutions offers a viable, cost-efficient method for the photocatalytic degradation of RhB, and this prototype has the potential to inspire the development of novel photocatalysts, such as splitting water, reducing CO_2, and fixing N_2.

Data availability statement

The original contributions presented in the study are included in the article/supplementary material, further inquiries can be directed to the corresponding author.

Author contributions

WY and NG contributed to design of the study and organized the database. WY wrote the first draft of the manuscript. JH and WY wrote sections of the manuscript. All authors contributed to manuscript revision, read, and approved the submitted version.

Funding

This work was financially supported by funding from the National Natural Science Foundation of China (NSFC 51972207), Science and Technology Commission of Shanghai Municipality (No. 19DZ2271100), and Science and Technology Commission of Shanghai Municipality (No. 21ZR1425100).

Conflict of interest

The authors declare that the research was conducted in the absence of any commercial or financial relationships that could be construed as a potential conflict of interest.

Publisher's note

References

Albornoz, L. L., Bortolozzi, J. P., Banús, E. D., Brussino, P., da Silva, S. W., Bernardes, A. M., et al. (2021). Synthesis and characterization of immobilized titanium-zirconium Sn-doped oxides onto metallic meshes and their photocatalytic activity for erythromycin mineralization. *Chem. Eng. J.* 414, 128891. doi:10.1016/j.cej.2021.128891

Asokan, K., Park, J. Y., Choi, S., Chang, C., and Kim, S. S. (2010). Stabilization of the anatase phase of Ti1−x Sn x O2 (x. *Nano Res.* 3, 256–263. doi:10.1007/s12274-010-1028-y

Bjelajac, A., Petrović, R., Djokic, V., Matolin, V., Vondraček, M., Dembele, K., et al. (2018). Enhanced absorption of TiO2 nanotubes by N-doping and CdS quantum dots sensitization: Insight into the structure. *RSC Adv.* 8, 35073–35082. doi:10.1039/c8ra06341a

Chang, J., Jiang, Z. Y., Zhang, Z. Y., Lin, Y. M., Tian, P. L., Zhou, B., et al. (2019). Theoretical studies of photocatalytic behaviors of isoelectronic C/Si/Ge/Sn-doped TiO2: Dft + U. *Appl. Surf. Sci.* 484, 1304–1309. doi:10.1016/j.apsusc.2018.12.252

Chen, H., Tian, P., Fu, L., Wan, S., and Liu, Q. (2022). Hollow spheres of solid solution Fe7Ni3S11/CN as advanced anode materials for sodium ion batteries. *Chem. Eng. J.* 430, 132688. doi:10.1016/j.cej.2021.132688

Chen, L. C., Huang, C. M., Hsiao, M. C., and Tsai, F. R. (2010). Mixture design optimization of the composition of S, C, SnO2-codoped TiO2 for degradation of phenol under visible light. *Chem. Eng. J.* 165, 482–489. doi:10.1016/j.cej.2010.09.044

Fan, H., Wang, R., Xu, Z., Duan, H., and Chen, D. (2021). Migration and enrichment behaviors of Ca and Mg elements during cooling and crystallization of boron-Bearing titanium slag melt. *Crystals* 11, 888. doi:10.3390/cryst11080888

Fan, W., Yu, X., Lu, H. C., Bai, H., Zhang, C., and Shi, W. (2016). Fabrication of TiO2/RGO/Cu2O heterostructure for photoelectrochemical hydrogen production. *Appl. Catal. B Environ.* 181, 7–15. doi:10.1016/j.apcatb.2015.07.032

Galvão, T. L., Sousa, I., Wilhelm, M., Carneiro, J., Opršal, J., Kukačková, H., et al. (2018). Improving the functionality and performance of AA2024 corrosion sensing coatings with nanocontainers. *Chem. Eng. J.* 341, 526–538. doi:10.1016/j.cej.2018.02.061

Golestanbagh, M., Parvini, M., and Pendashteh, A. (2018). Preparation, characterization and photocatalytic properties of visible-light-driven CuO/SnO2/TiO2 photocatalyst. *Catal. Lett.* 148, 2162–2178. doi:10.1007/s10562-018-2385-5

González-Gutiérrez, A. G., Pech-Canul, M. A., Chan-Rosado, G., and Sebastian, P. J. (2019). Studies on the physical and electrochemical properties of Ni-P coating on commercial aluminum as bipolar plate in PEMFC. *Fuel* 235, 1361–1367. doi:10.1016/j.fuel.2018.08.104

Huang, M., Yu, J., Li, B., Deng, C., Wang, L., Wu, W., et al. (2015). Intergrowth and coexistence effects of TiO2-SnO2 nanocomposite with excellent photocatalytic activity. *J. Alloys Compd.* 629, 55–61. doi:10.1016/j.jallcom.2014.11.225

Kong, L., Guo, J., Makepeace, J. W., Xiao, T., Greer, H. F., Zhou, W., et al. (2019). Rapid synthesis of BiOBrxI1-x photocatalysts: Insights to the visible-light photocatalytic activity and strong deviation from Vegard's law. *Catal. Today* 335, 477–484. doi:10.1016/j.cattod.2019.02.013

Li, Y., Zhang, J., Chen, Q., Xia, X., and Chen, M. (2021). Emerging of heterostructure materials in energy storage: A review. *Adv. Mat.* 33, 2100855. doi:10.1002/adma.202100855

Liang, J., Wei, W., Zhong, D., Yang, Q., Li, L., and Guo, L. (2012). One-step *in situ* synthesis of SnO2/graphene nanocomposites and its application as an anode material for Li-ion batteries. *ACS Appl. Mat. Interfaces* 4, 454–459. doi:10.1021/am201541s

Liu, C., Zhang, Q., and Zou, Z. (2023). Recent advances in designing ZnIn2S4-based heterostructured photocatalysts for hydrogen evolution. *J. Mater. Sci. Technol.* 139, 167–188. doi:10.1016/j.jmst.2022.08.030

Liu, C., Zhang, Y., Wu, J., Dai, H., Ma, C., Zhang, Q., et al. (2022). Ag-Pd alloy decorated ZnIn2S4 microspheres with optimal Schottky barrier height for boosting visible-light-driven hydrogen evolution. *J. Mater. Sci. Technol.* 114, 81–89. doi:10.1016/j.jmst.2021.12.003

Liu, J., Zhao, Z., Xu, C., and Liu, J. (2019). Structure, synthesis, and catalytic properties of nanosize cerium-zirconium-based solid solutions in environmental catalysis. *Chin. J. Catal.* 40, 1438–1487. doi:10.1016/s1872-2067(19)63400-5

Liu, Y., Yao, W., Wang, G., Wang, Y., Moita, A. S., Han, Z., et al. (2016). Reversibly switchable wettability on aluminum alloy substrate corresponding to different pH droplet and its corrosion resistance. *Chem. Eng. J.* 303, 565–574. doi:10.1016/j.cej.2016.06.038

Long, R., Dai, Y., Meng, G., and Huang, B. (2009). Energetic and electronic properties of X- (Si, Ge, Sn, Pb) doped TiO2 from first-principles. *Phys. Chem. Chem. Phys.* 11, 8165–8172. doi:10.1039/b903298c

Luo, M., Xu, Y. E., and Song, Y. X. (2018). Modulation of band gap by normal strain in SiC-based heterostructures. *Optik* 154, 634–639. doi:10.1016/j.ijleo.2017.10.044

Mohammad, A., Khan, M. E., Cho, M. H., and Yoon, T. (2021). Fabrication of binary SnO2/TiO2 nanocomposites under a sonication-assisted approach: Tuning of band-gap and water depollution applications under visible light irradiation. *Ceram. Int.* 47, 15073–15081. doi:10.1016/j.ceramint.2021.02.065

Nuansing, W., Ninmuang, S., Jarernboon, W., Maensiri, S., and Seraphin, S. (2006). Structural characterization and morphology of electrospun TiO2 nanofibers. *Mater. Sci. Eng. B* 131, 147–155. doi:10.1016/j.mseb.2006.04.030

Pelicano, C. M., Saruyama, M., Takahata, R., Sato, R., Kitahama, Y., Matsuzaki, H., et al. (2022). Bimetallic synergy in ultrafine cocatalyst alloy nanoparticles for efficient photocatalytic water splitting. *Adv. Funct. Mater.* 32, 2202987. doi:10.1002/adfm.202202987

Prasad, L. C., and Mikula, A. (2000). Concentration fluctuations and interfacial adhesion at the solid-liquid interface between Al2O3 and al-Sn liquid alloys. *High. Temp. Mat. Process.* 19, 61–69. doi:10.1515/htmp.2000.19.1.61

Pudukudy, M., Yaakob, Z., Mazuki, M. Z., Takriff, M. S., and Jahaya, S. S. (2017). One-pot sol-gel synthesis of MgO nanoparticles supported nickel and iron catalysts for undiluted methane decomposition into COx free hydrogen and nanocarbon. *Appl. Catal. B Environ.* 218, 298–316. doi:10.1016/j.apcatb.2017.04.070

Qin, Q., Wang, J., Xia, Y., Yang, D., Zhou, Q., Zhu, X., et al. (2021). Synthesis and characterization of Sn/Ni single doped and Co-doped anatase/rutile mixed-crystal nanomaterials and their photocatalytic performance under UV-visible light. *Catalysts* 11, 1341. doi:10.3390/catal11111341

Reddy, B. M., Saikia, P., and Bharali, P. (2008). Highly dispersed Ce x Zr1−x O2 nano-oxides over alumina, silica and titania supports for catalytic applications. *Catal. Surv. Asia* 12, 214–228. doi:10.1007/s10563-008-9053-5

Ren, B., Jin, Q., Li, Y., Li, Y., Cui, H., and Wang, C. (2020). Activating titanium dioxide as a new efficient electrocatalyst: From theory to experiment. *ACS Appl. Mat. Interfaces* 12, 11607–11615. doi:10.1021/acsami.9b21575

Ruiz Esquius, J., Algara-Siller, G., Spanos, I., Freakley, S. J., Schlögl, R., and Hutchings, G. J. (2020). Preparation of solid solution and layered IrOx-Ni(OH) 2 oxygen evolution catalysts: Toward optimizing iridium efficiency for OER. *ACS Catal.* 10, 14640–14648. doi:10.1021/acscatal.0c03866

Sayılkan, F., Asiltürk, M., Tatar, P., Kiraz, N., Şener, Ş., Arpaç, E., et al. (2008). Photocatalytic performance of Sn-doped TiO2 nanostructured thin films for photocatalytic degradation of malachite green dye under UV and VIS-lights. *Mater. Res. Bull.* 43, 127–134. doi:10.1016/j.materresbull.2007.02.012

Sayılkan, H. (2007). Improved photocatalytic activity of Sn4+-doped and undoped TiO2 thin film coated stainless steel under UV- and VIS-irradiation. *Appl. Catal. A General* 319, 230–236. doi:10.1016/j.apcata.2006.12.012

Serpone, N. (2006). Is the band gap of pristine TiO2 narrowed by anion- and cation-doping of titanium dioxide in second-generation photocatalysts? *J. Phys. Chem. B* 110, 24287–24293. doi:10.1021/jp065659r

Sharon, M., Modi, F., Modi, M., and Sharon, M. (2016). Titania based nanocomposites as a photocatalyst: A review. *Mat. Sci.* 3, 1236–1254. doi:10.3934/matersci.2016.3.1236

Shi, Z. M., Yan, L., Jin, L. N., Lu, X. M., and Zhao, G. (2007). The phase transformation behaviors of Sn2+-doped Titania gels. *J. Non-Crystalline Solids* 353, 2171–2178. doi:10.1016/j.jnoncrysol.2007.02.048

Singh, A., Sikarwar, S., Verma, A., and Chandra Yadav, B. C. (2021). The recent development of metal oxide heterostructures based gas sensor, their future opportunities and challenges: A review. *Sensors Actuators A Phys.* 332, 113127. doi:10.1016/j.sna.2021.113127

Wang, P., Song, T., Gao, G., Matras-Postolek, K., and Yang, P. (2022). SnO2 clusters embedded in TiO2 nanosheets: Heterostructures and gas sensing performance. *Sensors Actuators B Chem.* 357, 131433. doi:10.1016/j.snb.2022.131433

Wu, L., Yan, H., Li, X., and Wang, X. (2017). Characterization and photocatalytic properties of SnO 2 -TiO 2 nanocomposites prepared through gaseous detonation method. *Ceram. Int.* 43, 1517–1521. doi:10.1016/j.ceramint.2016.10.124

Wu, Y., Chen, Y., Li, D., Sajjad, D., Chen, Y., Sun, Y., et al. (2022). Interface engineering of organic-inorganic heterojunctions with enhanced charge transfer. *Appl. Catal. B Environ.* 309, 121261. doi:10.1016/j.apcatb.2022.121261

Yu, D. G., Li, J. J., Williams, G. R., and Zhao, M. (2018). Electrospun amorphous solid dispersions of poorly water-soluble drugs: A review. *J. Control. Release* 292, 91–110. doi:10.1016/j.jconrel.2018.08.016

Zhao, S., Huang, J., Huo, Q., Zhou, X., and Tu, W. (2016). A non-noble metal MoS2-Cd0.5Zn0.5S photocatalyst with efficient activity for high H2 evolution under visible light irradiation. *J. Mat. Chem. A* 4, 193–199. doi:10.1039/C5TA08365F